Computational Particle Mechanics
https://doi.org/10.1007/s40571-024-00894-w

A comparative study of JKR and DMT contact models for the DEM simulation of powder spreading in additive manufacturing

Sujith Reddy Jaggannagari[1] · Yixiang Gan[2] · Ratna Kumar Annabattula[1,3]

Received: 5 March 2024 / Revised: 14 December 2024 / Accepted: 19 December 2024
© The Author(s) under exclusive licence to OWZ 2025

Abstract
Powder spreading is the fundamental and most important process of powder bed fusion additive manufacturing. Powder particles experience cohesive forces due to their micron size, and these forces influence the quality of the layer. The dynamics of powder spreading is simulated using the discrete element method (DEM). DEM contact models with non-cohesive and cohesive interactions were used in past studies. This work compares two predominant cohesion contact models, the Johnson–Kendall–Roberts (JKR) and Derjaguin–Muller–Toporov (DMT). The influence of cohesion parameters and particle size on the spread layer quality is analysed. Additionally, mesoscopic analysis is carried out to gain insights into the behaviour of the spreading mechanism. The Tabor parameter (λ_T) that establishes the suitability of a specific cohesion model is investigated in the context of powder spreading process. Both models predict similar packing fractions at lower λ_T, whereas, at higher values of the λ_T, the contact forces of the JKR and DMT models diverge, leading to differences in packing fractions and local particle configurations in the spread layer. The findings demonstrate that the JKR model is applicable across the entire range of Tabor parameter.

Keywords Cohesion contact models · Discrete element method (DEM) · Derjaguin–Muller–Toporov model (DMT) · Johnson–Kendall–Roberts model (JKR) · Powder bed fusion additive manufacturing (PBFAM)

1 Introduction

Powder bed fusion additive manufacturing (PBFAM) technique has been used extensively to manufacture/fabricate a wide range of components starting from mechanical [1, 2] to aircraft [3, 4] to bio-medical implants [5]. The components can be built by spreading powders and selectively fusing them with a laser beam in a layer-by-layer manner. The structural and thermo-mechanical characteristics of these components depend not only on the powder bed layer [6, 7], but also on factors such as the heating source [8], melting [9, 10], and solidification rates [11]. Therefore, the analysis of the powder bed, melting, and solidification rates is crucial for the production of high-quality parts and the optimisation of production efficiency. Among the above processes, the generation of a dense powder bed is a fundamental and crucial step in PBFAM, as the quality of the powder bed dictates the overall quality of the finished parts [12].

The ability of the powder to form a quality layer (thin, dense, and without voids) depends on the rheological properties of powders. The metal powders for PBFAM are micron-sized, have a spherical and non-spherical shape (see Fig. 1a), and often exhibit a particle size distribution that closely resembles a Gaussian distribution (see Fig. 1b). The atomisation process produces the powder with irregular shapes and rough surfaces, as illustrated in Fig. 1c, d. The non-spherical particles experience unique interparticle interaction forces, influencing the powder flow dynamics. Furthermore, due to their smaller size, the van der Waals force dominates the interparticle interactions, in addition to

✉ Ratna Kumar Annabattula
ratna@iitm.ac.in

Sujith Reddy Jaggannagari
sujithreddyiitm@gmail.com

Yixiang Gan
yixiang.gan@sydney.edu.au

1 Mechanics of Materials Laboratory, Department of Mechanical Engineering, Indian Institute of Technology Madras, Chennai 600036, India

2 School of Civil Engineering, The University of Sydney, Sydney, NSW 2006, Australia

3 Additive Manufacturing Group, Centre of Excellence in Materials and Manufacturing for Futuristic Mobility, Indian Institute of Technology Madras, Chennai 600036, India

Published online: 17 February 2025

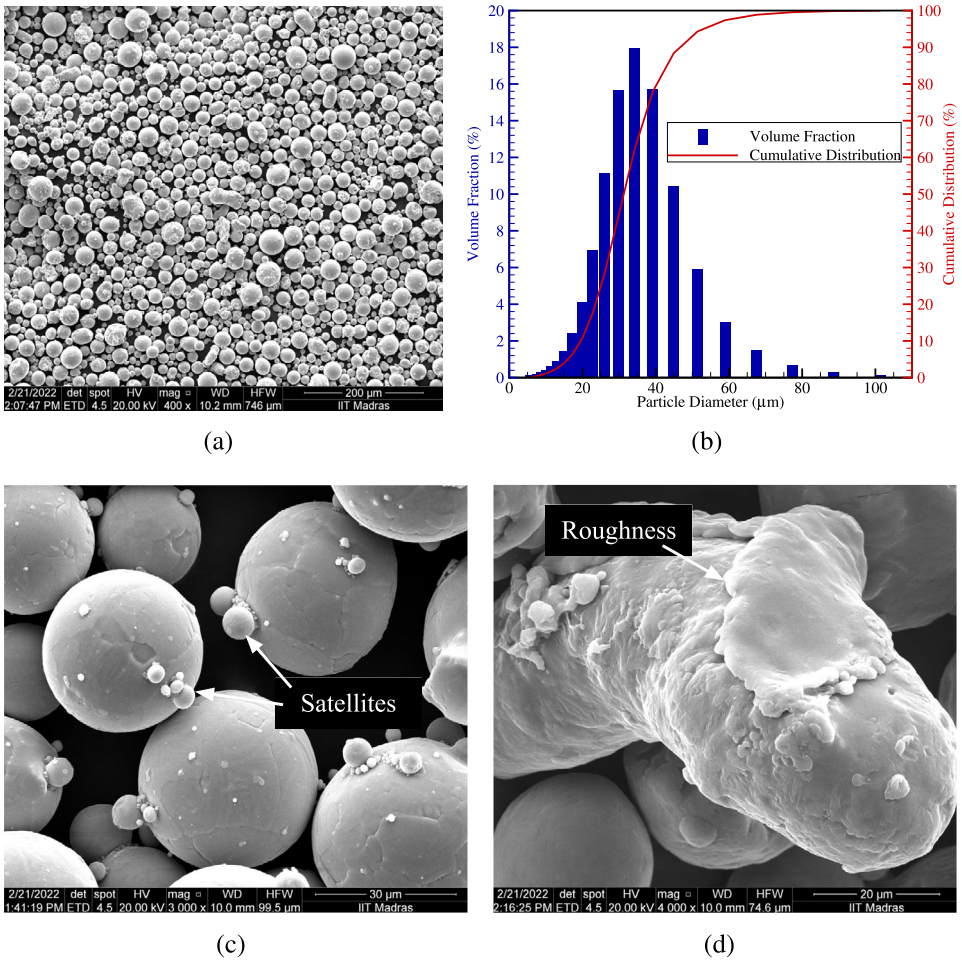

Fig. 1 **a** Scanning electron microscope (SEM) image of stainless steel 316L powder showing spherical and non-spherical particles with **b** particle size distribution (PSD) measured using particle size analyser. $D_{10} = 19.5\,\mu\text{m}$, $D_{50} = 32.42\,\mu\text{m}$, $D_{90} = 46.6\,\mu\text{m}$, SEM images of **c** Ti6Al4V powder particle showing satellite irregularities and **d** AlSi10Mg powder particle showing surface roughness irregularities

the elastic, frictional, and gravitational forces, thereby influencing the powder layer quality [6, 13, 14]. The experimental measurement of these forces and the powder bed layer analysis remain persistent challenges. Therefore, it is crucial that the numerical models account for all these relevant interactions between particles to study the powder flow dynamics accurately in PBFAM. Numerical simulations ensure a realistic representation of the powder bed and are instrumental in optimising the process parameters responsible for producing high-quality PBFAM products.

In this paper, the powder flow dynamics during spreading is simulated using the discrete element method (DEM) [6, 15–22]. DEM is an efficient numerical tool to model particle–particle and particle–geometry interactions for granular materials [23]. The contact models in DEM are the key to accurately representing particle interactions and predicting their behaviour in granular systems. The DEM contact model specifies the forces and torques acting on particles when they come into contact with other particles or geometry [24–27], the details of which are described in Sect. 2. Contact models will facilitate a more thorough comprehension of the correlation between micro- and macromechanics.

In previous studies, various contact models are used to simulate the powder spreading process, as tabulated in Table 1. Contact models such as the linear elastic adhesive law [20], Lennard–Jones potential [28], linear Hookean [29, 30], Johnson–Kendall–Roberts (JKR) [15, 16, 18, 19, 30–33], and Derjaguin–Muller–Toporov (DMT) [6, 17, 34–36] are used to model powder spreading processes. Furthermore, researchers have investigated powders with different particle size distributions, characterised by a range of varying mean particle sizes and material properties (see Table 1). By utilising powders with diverse size distributions, these studies aim to explore the influence of particle size on key phenomena such as flowability and spreadability, as outlined in Table 1.

It is evident from the literature that powder spreading simulations were conducted with various contact models (see Table 1). Among several cohesion contact models developed to describe the cohesive interaction between particles, the JKR and DMT models are predominantly used. JKR contact model is valid for large particles with low elastic modulus (soft) and high surface energy, whereas DMT model is suitable for small particles with high elastic modulus (hard) and low surface energy. Both the JKR and DMT models offer

Table 1 List of powders, particle sizes, and contact models used in previous studies

References	Powders	Size range (μm)	Mean size (μm)	Surface energy (mJ/m^2)	Young's modulus (Gpa)	Contact model
Shaheen et al. [20]	Ti6Al4V	12–79	–	0–0.4	–	A linear elastic adhesive force law
Wang et al. [28]	Ni-alloy	5–65	34	*$0.1-10e-20$	1	Lennard–Jones potential
Haeri et al. [29]	Poly-Ether Ether Ketone (PEEK)	Mono-sized	50	–	–	Linear Hookean spring-dashpot model
Gao et al. [37]	316L stainless steel	20–100	50	0.001	2.2	JKR
Yao et al. [19]	316L stainless steel	Mono-sized	50	0.1–2	0.22	JKR
Chen et al. [31]	Steel powder	Mono-sized	50	0–17	22	JKR
Chen et al. [15]	316L stainless steel	53–96, 0–62	–	0.097	2.2	JKR
Nan et al. [32]	316L stainless steel	15–55	–	1.4	2.1	JKR
Han et al. [30]	HX alloy powder	15–55	35	0–2	2	JKR
Wu et al. [18]	2195 Al Alloy	2.2–90	–	0.2	75	JKR
Wu et al. [33]	Ti6Al4V	13–86	–	0.75	0.44	JKR
Meier et al. [34]	Ti6Al4V	–	34	0–0.4	–	DMT
Yuksel and Cullinan [35]	–	0.025–0.175	0.1	*$0-28e-20$	–	DMT
Parteli and Poschel [6]	–	10–95	–	0.1	0.023	DMT

*Hamaker constant (H_a) of DMT model in J

valuable insights into the behaviour of particles with cohesive contact interactions and have been extensively employed in various fields, including nanosystems, tribology, and medical sciences [38–41]. In the past studies, JKR and DMT models were applied to a wide range of powder types. Parteli et al. [13] investigated the packing density of fine glass powders using JKR and DMT models to account for cohesive particle interactions. Behjani et al. [42] simulated the granulation process of calcium carbonate powders using the JKR contact model to study the flow and mixing behaviour of the particles during granulation. Pizette et al. [43] explored the factors influencing the green strength of binder-free ceramic powders using DEM simulations with the DMT model. Behjani et al. [44] used the JKR model to study the blending process of pharmaceutical powders in a continuous twin-screw mixer, highlighting the model's ability to handle cohesive powder systems in pharmaceutical applications. The JKR contact model is commonly used in investigating powder spreading systems, while the DMT model is less frequently used. However, there is still some ambiguity regarding the suitability of JKR or DMT models for the realistic simulation of powder spreading. This work investigates the powder spreading process of spherical particles incorporating JKR and DMT cohesion contact models. The effect of cohesion parameters and non-contact interactions on powder flow and the powder layer quality generated by the spreading process is analysed for both contact models. The objectives of this work are to provide answers to the following questions regarding the modelling of PBFAM spreading.

1. What are the noticeable differences in the powder layer formed during spreading using the JKR, DMT, and non-cohesive Hertz–Mindlin (HM) contact models?
2. What are the effects of cohesion parameters and the particle size distribution on the quality of the spread layer?
3. What is the particle's mechanical and cohesion property range suitable for the use of JKR and DMT cohesion models?

A detailed approach to address the above questions is presented in the following. A description of the simulation methodology with different contact models and details of the DEM simulations carried out are given in Sect. 2. The results and discussion regarding the influence of cohesion parameters and particle size variations on the spread powder layer are reported in Sects. 3.1 and 3.2. Further, the respective range of suitability of cohesion models using Tabor's parameter is presented in Sect. 3.3. Finally, Sect. 4 summarises the paper.

2 Methodology

In this section, the DEM framework with three different contact models (HM, JKR, and DMT) is presented to investigate their respective roles in the powder spreading process for PBFAM. A comparative analysis of cohesion models to address both contact and non-contact based interactions is also presented. Furthermore, a non-dimensional Tabor parameter is introduced to ascertain the suitability of a specific cohesion model for the range of system properties considered in this work.

2.1 DEM framework and contact models

The discrete nature of the powder particles is modelled using DEM, which treats each individual particle as a distinct entity. In DEM, the translational and rotational motions of the particles are governed by Newton's second law of motion and the governing equations are delineated below:

$$m_i \frac{\mathrm{d}\boldsymbol{v}_i}{\mathrm{dt}} = \sum_j (\boldsymbol{F}^{\mathrm{n}}_{ij} + \boldsymbol{F}^{\mathrm{t}}_{ij}) + m_i \boldsymbol{g} \tag{2.1}$$

$$I_i \frac{\mathrm{d}\boldsymbol{\omega}_i}{\mathrm{dt}} = \sum_j (\boldsymbol{T}^{\mathrm{t}}_{ij} + \boldsymbol{T}^{\mathrm{r}}_{ij}) \tag{2.2}$$

where m_i, $\boldsymbol{v}_i$, I_i, and $\boldsymbol{\omega}_i$ are the mass, velocity, moment of inertia, and angular velocity of the particle i, respectively. $\boldsymbol{F}^{\mathrm{n}}_{ij}$ and $\boldsymbol{F}^{\mathrm{t}}_{ij}$ are the normal and tangential contact forces between particle i and j.[1] $\boldsymbol{T}^{\mathrm{t}}_{ij}$ and $\boldsymbol{T}^{\mathrm{r}}_{ij}$ denote the contact torque due to the tangential contact forces and rolling resistance. Further, the normal and tangential contact forces can be additively decomposed according to

$$\boldsymbol{F}^{\mathrm{n}}_{ij} = \boldsymbol{F}^{\mathrm{n,c}}_{ij} + \boldsymbol{F}^{\mathrm{n,d}}_{ij} \tag{2.3}$$

$$\boldsymbol{F}^{\mathrm{t}}_{ij} = \boldsymbol{F}^{\mathrm{t,c}}_{ij} + \boldsymbol{F}^{\mathrm{t,d}}_{ij} \tag{2.4}$$

The Hertz–Mindlin is a cohesion-less, nonlinear elastic contact model [45]. In this model, the normal ($\boldsymbol{F}^{\mathrm{n}}_{ij}$) and tangential force ($\boldsymbol{F}^{\mathrm{t}}_{ij}$) components are based on Hertzian contact theory [45] and Mindlin–Deresiewicz [46], respectively. The contact normal ($\boldsymbol{F}^{\mathrm{n,c}}_{ij}$) and tangential ($\boldsymbol{F}^{\mathrm{t,c}}_{ij}$) forces depend on the positive normal overlap (δ^{n}_{ij}) (see Fig. 2a), as expressed in Eq. (2.5). The JKR model considers the van der Waals force of attraction to describe the cohesive behaviour of metal powders [47]. The normal contact force in the JKR model and the relationship between the contact radius (r_{c}) and the overlap (δ^{n}_{ij}) are given in Eq. (2.6) (see Fig. 2a). The normal contact force of the DMT model is provided in Eq. (2.7) [48, 49]. The expressions for the normal damping force ($\boldsymbol{F}^{\mathrm{n,d}}_{ij}$), tangential damping force ($\boldsymbol{F}^{\mathrm{t,d}}_{ij}$), tangential torque ($\boldsymbol{T}^{\mathrm{t}}_{ij}$), and rolling resistance torque ($\boldsymbol{T}^{\mathrm{r}}_{ij}$) are the same for all the three contact models discussed in this section. The exact formulation for the estimation of $\boldsymbol{F}^{\mathrm{n,d}}_{ij}$, $\boldsymbol{F}^{\mathrm{t,d}}_{ij}$, $\boldsymbol{T}^{\mathrm{t}}_{ij}$, $\boldsymbol{T}^{\mathrm{r}}_{ij}$ is detailed in the supplementary information.

$$\text{HM} \left\{ \begin{array}{lcl} \boldsymbol{F}^{\mathrm{n,c}}_{ij} & = & \dfrac{4}{3} E^* \sqrt{R^*}\, (\delta^{\mathrm{n}}_{ij})^{\frac{3}{2}} \hat{\boldsymbol{n}} \\ \boldsymbol{F}^{\mathrm{t,c}}_{ij} & = & 8 G^* \sqrt{R^* \delta^{n}_{ij}}\, \delta^{\mathrm{t}}_{ij} \hat{\boldsymbol{n}} \\ \delta^{\mathrm{n}}_{ij} & = & |\boldsymbol{x}_{\mathrm{i}} - \boldsymbol{x}_{\mathrm{j}}| - (r_i + r_j) \end{array} \right\} \tag{2.5}$$

$$\text{JKR} \left\{ \begin{array}{l} \boldsymbol{F}^{\mathrm{n,c}}_{ij} = \dfrac{4E^*}{3R^*} r_{\mathrm{c}}^3 \hat{\boldsymbol{n}} - \sqrt{8\pi E^* \Gamma}\; r_{\mathrm{c}}^{\frac{3}{2}} \hat{\boldsymbol{n}} \\ r_{\mathrm{c}}^4 - 2\delta^{n}_{ij} R^*\, r_{\mathrm{c}}^2 - \dfrac{2\pi \Gamma R^{*2}}{E^*} r_{\mathrm{c}} + {\delta^{n}_{ij}}^2 R^{*2} = 0 \end{array} \right\} \tag{2.6}$$

$$\text{DMT} \left\{ \begin{array}{ll} \boldsymbol{F}^{\mathrm{n,c}}_{ij} = 0 & \text{if} \quad \delta^{\mathrm{n}}_{ij} < -\delta^{n}_{\text{cut-off}} \\ \boldsymbol{F}^{\mathrm{n,c}}_{ij} = -\dfrac{H_{\mathrm{a}} R^*}{6\left(\delta^{\mathrm{n}}_{ij}\right)^2} \hat{\boldsymbol{n}} & \text{if} \quad -\delta^{n}_{\text{cut-off}} \le \delta^{\mathrm{n}}_{ij} < -\delta_{\min} \\ \boldsymbol{F}^{\mathrm{n,c}}_{ij} = -\dfrac{H_{\mathrm{a}} R^*}{6\delta^2_{\min}} \hat{\boldsymbol{n}} & \text{if} \quad -\delta_{\min} \le \delta^{\mathrm{n}}_{ij} < 0 \\ \boldsymbol{F}^{\mathrm{n,c}}_{ij} = \dfrac{4}{3} E^* \sqrt{R^*}\, (\delta^{\mathrm{n}}_{ij})^{\frac{3}{2}} \hat{\boldsymbol{n}} - \dfrac{H_{\mathrm{a}} R^*}{6\delta^2_{\min}} \hat{\boldsymbol{n}} & \text{if} \quad \delta^{\mathrm{n}}_{ij} \ge 0 \end{array} \right\} \tag{2.7}$$

Here, E^*, R^*, δ^{n}_{ij}, δ^{t}_{ij}, $\hat{\boldsymbol{n}}$, r_{c}, r_i, $\boldsymbol{x}_i$, H_{a} are the effective Young's modulus, effective radius, normal overlap, tangential overlap, unit normal vector, contact radius, radius, position, and Hamaker constant of the particles, respectively (refer supplementary material for details). Additionally, $\delta_{\min}$ is the minimum atomic separation distance between particles, usually considered to be 1.65 Å [13, 50]. For the particles of the same material, the work of adhesion $\Gamma = 2\gamma$, where γ is the surface energy of the particles.

The distinction between the JKR and DMT contact models in terms of their interaction is briefly outlined in the following discussion. At the contact level, two interacting particles have different levels of engagement during the loading (particles coming closer together) and unloading (particles moving farther apart) stages. In the loading stage, two particles may undergo non-contact interaction (negative δ^{n}_{ij}), followed by contact interaction (positive δ^{n}_{ij}) as shown in Fig. 2b with blue particles. Conversely, in the unloading stage, the interaction between these two particles proceeds from contact interaction to non-contact interaction, as described by the red particles in Fig. 2b. The characteristic curve of the JKR model is shown in Fig. 2c, d show the characteristic curves for

[1] Note that i and j represent the particles indices and do not represent the indices of a second-order tensor.

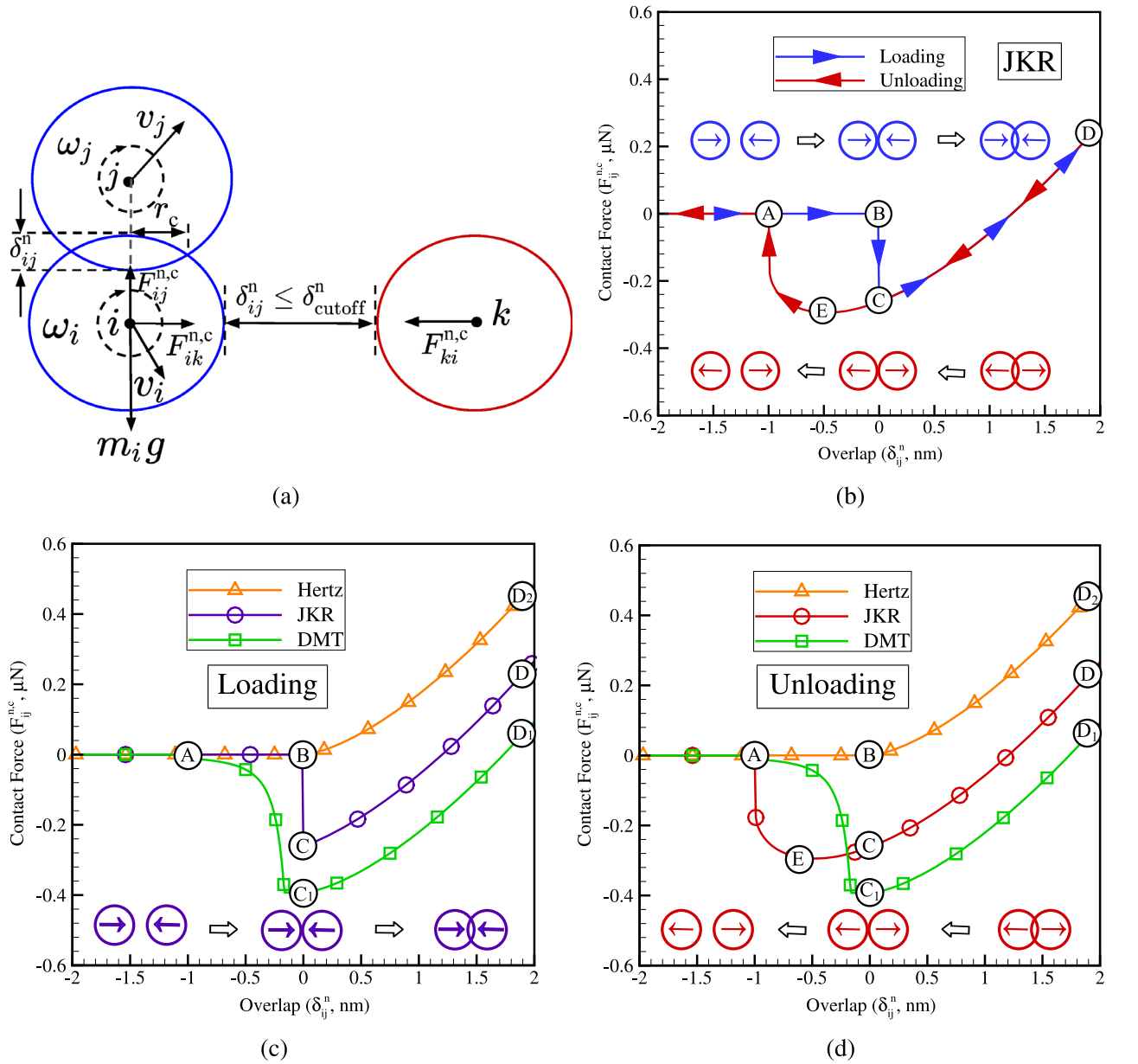

Fig. 2 **a** Schematic illustration of the forces acting on the particles, **b** Characteristic curve of the JKR model for two-particle interaction. The distinctions in the characteristic curves of the Hertz, JKR, and DMT models during **c** loading and **d** unloading stage

the HM, JKR, and DMT models in the loading, and unloading stages. In the loading stage, the JKR model does not consider non-contact interactions (as shown in Fig. 2c). The normal contact force drops from point B to C due to the cohesion forces at the zero overlap. During the contact interactions, the normal force is lower than the Hertzian contact force (compare points D and D_2), as shown in Fig. 2c. During the unloading stage, particles experience non-contact van der Waals forces. The maximum cohesive force called the pull-out force occurs at point (E) in the JKR model as shown in Fig. 2c and is given by Equation (2.8). Cut-off overlap is defined as the negative normal overlap beyond which the cohesive interaction breaks [27]. At this point, denoted as point (A), the non-contact cohesive interaction ceases, and cohesive forces are ignored once the negative normal overlap exceeds the cut-off overlap value given by Equation (2.9)

$$(\boldsymbol{F}_{ij}^{n,c})_{\text{pull-out}} = -3\pi\gamma R^{*}\hat{\boldsymbol{n}} \tag{2.8}$$

$$\delta_{\text{cut-off}}^{n} = -\left(\frac{3(\boldsymbol{F}_{ij}^{n,c})_{\text{pull-out}}^{2}}{16R^{*}E^{*2}}\right)^{\frac{1}{3}} \tag{2.9}$$

To establish a relevant comparison between the JKR and DMT models, the particle size, Young's modulus, and cut-

off overlap ($\delta^{n}_{\text{cut-off}}$) for both models are considered equal. In the DMT model, the Hamaker constant ($H_a = 24\pi\delta^2_{\min}\gamma$) is calculated with $\delta_{\min}$ = 1.65 Å, and surface energy (γ) equal to the JKR model. In the loading stage, the DMT model considers van der Waals forces within the cut-off overlap contrary to zero force in the case of the JKR model. As the two particles overlap, the contact forces in the DMT model are lower than those of the JKR, implying higher cohesive forces (compare points D and D_1 in Fig. 2c). As shown in Fig. 2d during the unloading phase, both the JKR and DMT models consider non-contact interactions, where the pull-out force for the JKR model (i.e. Point E) is manifested at a relatively larger separation distance than the DMT model (i.e. Point C_1). It should be noted that the DMT model (Eq. (2.10)) has higher pull-out forces than the JKR model (Eq. (2.8)).

$$(\boldsymbol{F}^{n,c}_{ij})_{\text{pull-out}} = -4\pi\gamma R^*\hat{\boldsymbol{n}} \tag{2.10}$$

2.2 Tabor parameter

The two well-established cohesion models, JKR and DMT, were initially considered competitive descriptions of adhesive interactions between solid surfaces [27]. However, subsequent research has revealed that these models represent the extreme limits within a specific range of solutions governed by a critical non-dimensional parameter known as the Tabor parameter (λ_T) [51]. It is the most critical parameter that considers the deformation of the particles that experience cohesive forces. The deformation of the particles with a diameter greater than 10 µm cannot be ignored [50]. In PBFAM, powder particles are above 10 µm, so modelling the powders must take into account the deformations of the particles. The Tabor parameter given by Equation (2.11) is the ratio of normal elastic deformation caused by cohesion to the spatial range of the cohesion forces. Figure 3 illustrates the induced elastic deformation (depicted by a contact circle of radius r_c) to a particle through the cohesive interaction (note that the particle and wall are separated by a distance of $\delta_{\min}$) with a wall [51]. According to Tabor, the JKR model is valid for $\lambda_T > 3$ and the DMT model is more appropriate for $\lambda_T < 0.1$ [27, 52–54]. The Maugis model is valid between the two limits, i.e. $0.1 < \lambda_T < 3$ [53]. In summary, selecting an appropriate cohesion model requires considering the material behaviour, contact range, and surface energies of the particles.

$$\boldsymbol{\lambda}_T = \left[\frac{4R^*\,\gamma^2}{E^{*2}\,\delta^3_{\min}}\right]^{1/3} \tag{2.11}$$

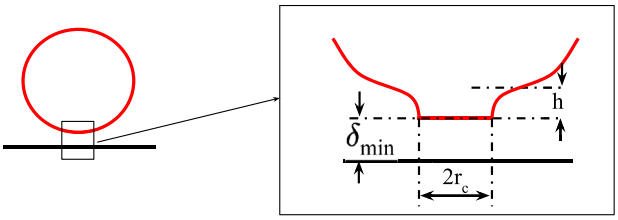

Fig. 3 Illustration of elastic deformation of a cohesive sphere and a wall [51]

2.3 Details of simulation set-up

This section describes the simulation procedure and the material properties used in this work. In most commercial PBFAM machines, blade-shaped flat recoaters are used. Therefore, powder spreading simulations are carried out using a blade recoater on the platform, and the homogeneity of the powder bed is analysed, as shown in Fig. 4a. The simulation set-up consists of two platforms: collection (L_c being its length) and spreading platform with length (L_s). The powder particles were generated at the left end of the collection platform. Subsequently, the generated particles were spread on the spreading platform with the recoater that moved along the x-direction at a constant speed (V) until the end of the spreading platform. The sufficient length of the collection platform is considered for the particles to become dynamic and develop a proper repose angle before reaching the spreading platform. The gap between the recoater and the spreading platform is known as the layer thickness (H). Periodic boundary conditions were applied across the width of the platform (along the y-direction), representing a very large (infinite) volume of the actual set-up by using a small volume similar to the representative volume element (RVE). Periodic boundary conditions ensure that particle interactions within the simulation domain represent the entire system. Additionally, the gravitational force is along the negative z-direction. Three zones are considered for subsequent analysis of the spreading process. Zone 1 to determine the deposition rate of the powder particles flowing through the gap between the recoater and the platform. Zone 2 for calculation of stress and coordination number of the particles in a pile in front of the recoater with an attached box bin, where the side length equals $8\times$ D_{50}. The packing fraction of the spread layer was analysed within Zone 3. The following sections will provide a comprehensive analysis of the metrics used to evaluate the powder spreading process. The material properties of the powder particles and the parameters considered for the simulations are provided in Table 2, assuming that the powder is 316 L stainless steel [32]. Nan et al. [32] provided detailed experimental investigations to determine the surface energy using a newly developed drop test method, which offers a robust approach to characterising surface energy values for various materials. Additionally,

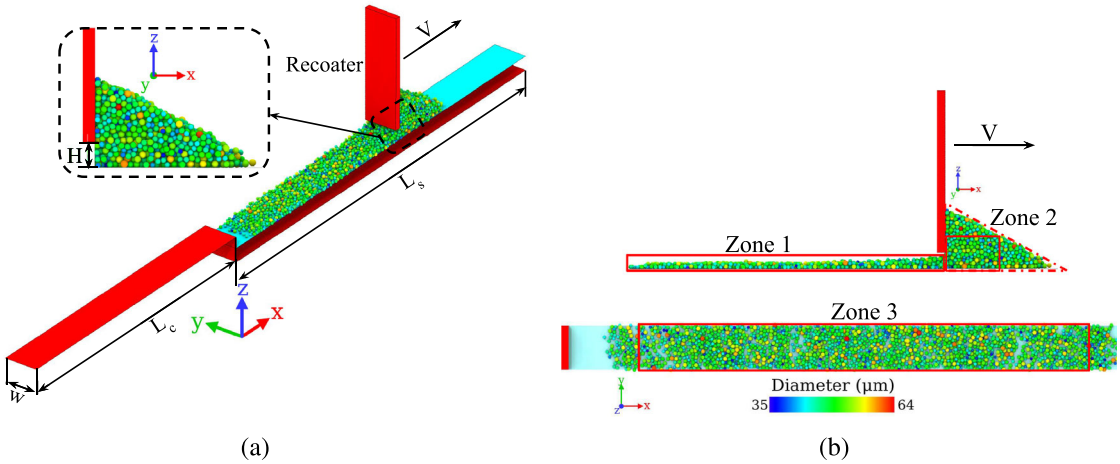

Fig. 4 Visualisation of the **a** powder spreading process **b** zones for analysis are highlighted

their work includes experimental techniques for determining key material properties such as Young's modulus, the coefficient of restitution, and the coefficient of sliding friction. The rolling friction coefficient considered is within range of values used in the literature [19, 20, 31]. The Young's modulus considered in the simulations is 100 times lower than the actual experimental value, and the surface energy is also correspondingly scaled down in accordance with the cohesion number [42, 50] (details in supplementary material). The analysis of the particle size distribution with varying mean size (D_m) and standard deviation (S_D) of the powder sizes is presented in Sects. 3.1 and 3.2. The simulations are carried out in EDEM [55], an Altair DEM tool. The contact models like Hertz–Mindlin and JKR with Hertz–Mindlin are available as built-in models in the tool. Altair EDEM^{TM} provides an application programming interface (API) to incorporate user-defined contact constitutive models. In this work, the DMT model is developed as an API for the comparative analysis of the three models to be discussed in the following.

3 Results and discussion

3.1 Effect of the mean powder size on the spread powder layer quality

The powders used in PBFAM exhibit a Gaussian distribution, as mentioned in Sect. 1. The powders with the Gaussian distribution of different mean sizes such as 25 μm, 50 μm, 75 μm, and 100 μm with the same standard deviation of the powder sizes (S_D = 5) are used for the simulation. Several spreading simulations have been carried out with varying surface energy (γ) of the particles and with HM, JKR, and DMT contact models. The layer thickness (H) is the most crucial process parameter that defines the quality of the spread layer.

Table 2 Material properties and simulation parameters

Parameters	Particles	Bed
Particle size (D, μm)	6–115	–
Young's modulus (E, GPa)	2.1	2.1
Poisson's ratio (ξ)	0.3	0.3
Coefficient of restitution (e)	0.64	0.64
Coefficient of static friction (μ_s)	0.5	0.5
Coefficient of rolling friction (μ_r)	0.1	0.1
Density (ρ, kg/m^3)	7980	–
Recoater velocity (V, m/s)	0.1	–
Layer thickness (H, μm)	$4D_m$	–
Length of the collection platform (L_c, mm)	–	5
Length of the spreading platform (L_s, mm)	–	7.5
Width of the spreading platform (W, mm)	–	0.6

For all simulations, the layer thickness is maintained to be four times the mean size ($4D_m$) so that the volume of the spreading zone increases with an increase in the mean size.

Model validation

In the current work, the dynamic repose angle (DRA) of the powder pile is used to validate the simulation results. DRA (θ) indicates powder flow during spreading, and a smaller repose angle signifies low cohesive powder and high powder flow. Figure 5 depicts the DRA for powder with the mean size of 25 μm is about 44.62° and 46.97° while spreading with JKR and DMT models, respectively. The powder with a mean size of 100 μm, θ is about 29.98° and 29.65° with JKR and DMT models, respectively. The DRA values of the powders with mean size 25 μm and 100 μm are in good agreement with the experiments and simulations studies in the literature

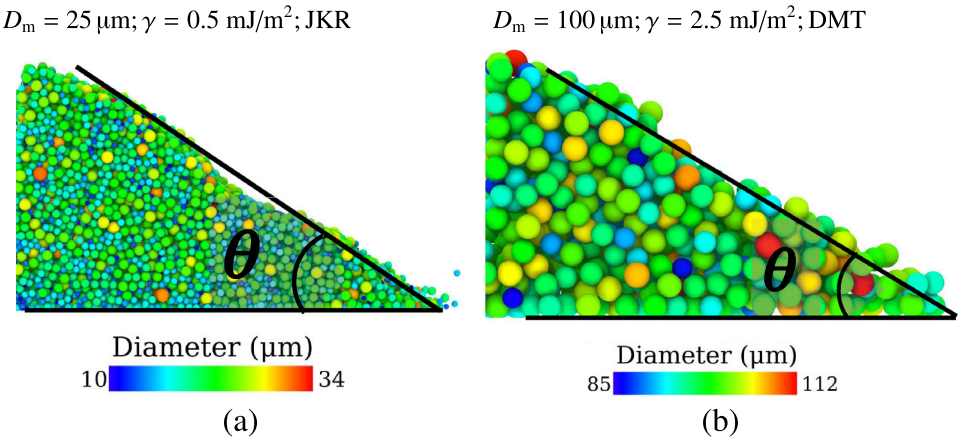

Fig. 5 Dynamic repose angle (θ) of powder pile during spreading process for powder with mean size (D_m) of **a** 25 µm, and **b** 100 µm

[12, 18, 19]. DRA for the powder with a smaller mean size is higher than that of a larger mean-sized powder because of higher cohesive forces.

3.1.1 Packing fraction and homogeneity of the powder layer

During the powder spreading, the powder pile is formed in front of the recoater, and the powder detached from the pile through the gap (H) forms a thin layer on the spreading platform. The terms flowability and spreadability are used in this context to characterise the ability of powders to flow and spread, respectively. Flowability characterises the extent to which a collection of particles moves in relation to neighbouring particles or along the recoater surface. It primarily impacts the detachment of particles from the piles and the replenishment of depleted regions within the piles [56]. Spreadability refers to the ability of a powder to be uniformly spread as a thin layer without any voids and agglomerates [21]. After the completion of the spreading process, a thin layer of powder is formed on the spreading platform (see Fig. 4b). The packing fraction of the spread layer has a direct impact on the quality of the final product produced through PBFAM. Therefore, the packing fraction of the spread layer is a crucial metric. The packing fraction of the thin layer is determined after the elimination of a few particle diameters at the extreme ends to avoid wall effects, as shown in zone 3 of Fig. 4b. The packing fraction is defined as the ratio of the total volume of the particles to the volume of the zone available for spreading and is given by the following:

$$\text{Packing fraction } (\phi) = \frac{\sum V_p}{L_s \times W \times H}, \tag{3.1}$$

where $\sum V_p$ is the total volume of the particles in the spread layer, and the definitions of L_s, W, and H are provided in Table 2.

The variation of the packing fraction of the spread layer as a function of surface energy (γ) with different mean sizes (as shown in Fig. 6a) and contact models is shown in Fig. 6b. The surface energy range considered in this study is based on values extracted from relevant literature, as presented in Table 1. HM contact model does not consider cohesion forces; thereby, the packing fraction of the spread powder layer is independent of the surface energy (solid lines in Fig. 6b). It is also observed that the packing fraction remains unchanged by variation in the mean particle size as the volume of the spreading zone increases with the mean size (i.e. $H = 4D_m$). It is a well-known fact in granular mechanics that the packing fraction is influenced by the relationship between the confinement volume and the size of the particles [57]. This is the reason to increase the layer thickness with respect to D_m. The objective is to study the effect of cohesion parameters and particle size on the spread powder layer rather than the effect of confinement volume. In reality, with the decrease in the mean size of the powders, the cohesive forces among the powder particles increase, leading to a poor powder bed. This phenomenon is well predicted by the cohesion models (JKR and DMT). Hence, the HM model is suitable for the investigation of the dynamics of powders with a mean size greater than 100 µm, as the powder particles experience lower cohesive forces, as shown in Fig. 6b. For the JKR and DMT models, the packing fraction of the bed decreases with a decrease in particle size for a given γ (dashed lines for JKR and dashed dots with marker lines for DMT in Fig. 6b). For a given particle size, it is observed that the packing fraction decreases with increasing γ as the cohesive force increases. The cohesive forces degrade the flowability and spreadability of the powder. Thus, the packing fraction of the powder layer decreases with decreasing particle size or increasing γ as shown in Fig. 6b. As explained in Sect. 2, the DMT model predicts higher cohesive forces than the JKR model, and the packing fraction obtained by the DMT model is always lower than the JKR model. Figure 7 shows the powder layers after spreading using the JKR contact model; it is observed that

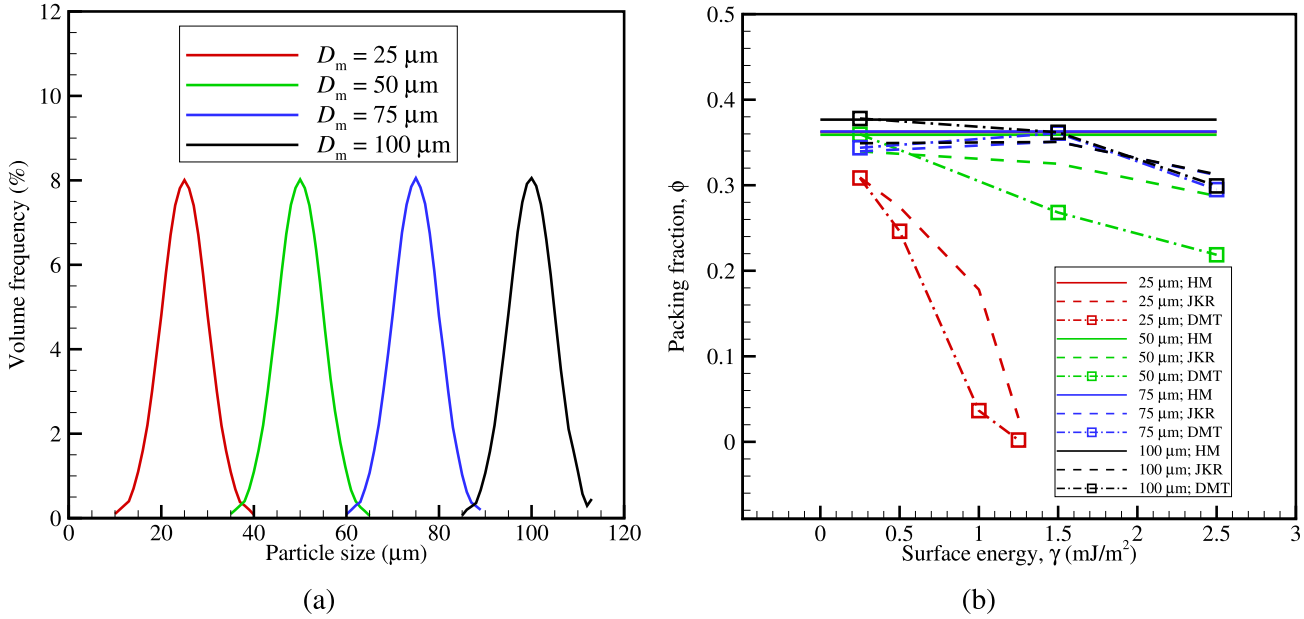

Fig. 6 **a** Particle size distribution with different mean sizes (D_m), **b** packing fraction (ϕ) variation as a function of the surface energy (γ)

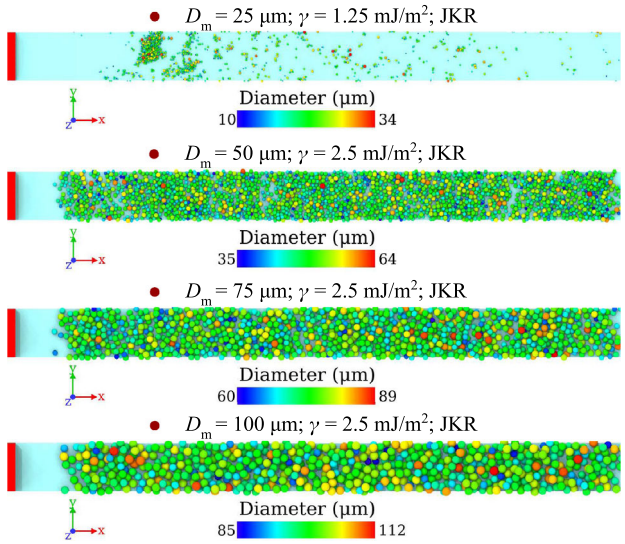

Fig. 7 Visualisation of the powder layer with variation of mean particle size (D_m)

the porosity increases (empty patches) with a decrease in the particle size (bottom to top images). The cohesive forces increase drastically for a relatively slight increase in surface energy for powders with a mean size (D_m) of 25 μm. Therefore, for γ that is equal to 1.25 mJ/m^2, the packing fraction of the spread layer approaches zero. It indicates that the powder forms agglomeration with no spreadability by spreading with a surface energy greater than 1.25 mJ/m^2. The subsequent section explains in detail the relationship between mesoscopic and macroscopic behaviour.

Mesoscopic analysis of the deposition mechanism

When the recoater spreads the powder on the spreading platform, the deposition of the powder on the platform is highly influenced by the stress distribution and the coordination number of the particles in the pile. These mesoscopic characteristics help to understand the effect of powder flow dynamics on powder deposition and bed quality. In the following section, the relationship between stress and the coordination number of the powder particles with the deposition rate is analysed. The metrics used to analyse the deposition rates, stress, and coordination number distribution are discussed below.

Deposition rate

During the spreading process, particles are released from the gap (H) between the recoater and the spreading platform and are deposited on the platform. The mass deposited between subsequent steps of spreading is shown as red-coloured particles in Fig. 8. The deposition rate (q) of the powder on the platform in zone 1 is calculated as $q = \frac{\mathrm{d}m}{\mathrm{d}t}$, where d$m$ is the mass of the particles deposited within a time interval $\mathrm{d}t = 0.001s$.

Stress and coordination number

The stress on the particles in a pile is calculated from zone 2 (see Fig. 8) at every time interval of deposition. The volume-averaged stress on the single discrete particle is calculated as follows:

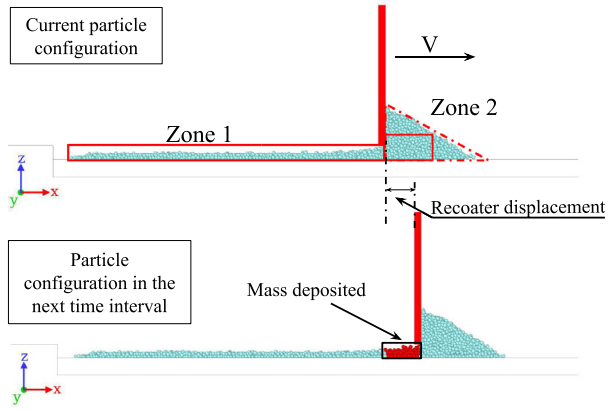

Fig. 8 Illustration of the mass deposition and recoater displacement

$$\boldsymbol{\sigma}_{\mathrm{ij}} = \frac{1}{V_{\mathrm{p}}}\left(\sum_{c=1}^{n_{\mathrm{c}}} \boldsymbol{F}_{\mathrm{ij}}^{\mathrm{c}} r_{\mathrm{ij}}^{\mathrm{c}}\right) \tag{3.2}$$

where V_{p} is the volume of the particle; n_{c} is the number of contacts of the particle; $\boldsymbol{F}_{\mathrm{ij}}^{\mathrm{c}}$ is the contact force at the contact c; and $r_{\mathrm{ij}}^{\mathrm{c}}$ is the corresponding vector connecting the centre of the particle i and j. The von Mises stress (σ_{v}) is computed from the stress tensor $\boldsymbol{\sigma}_{\mathrm{ij}}$. The coordination number (Z) of a particle is defined as the number of particles in contact and also non-contact particles within the cut-off overlap ($\delta_{\text{cut-off}}^{n}$).

Kernel smoothing density function

The amount of powder accumulated in front of the recoater decreases proportionally to the extent of powder deposition on the platform. Therefore, the average von Mises stress and coordination number values collected (from zone 2) at every time interval of deposition decrease from the beginning to the end of spreading. To quantify these varying quantities during the entire spreading process, a kernel smoothing density function is used. It provides local cloud density and is calculated as follows:

$$F(x) = \frac{1}{nh}\sum_{i=1}^{n} K\left(\frac{x - x_i}{h}\right) \tag{3.3}$$

where $F(x)$ is the probability density distribution, K is a normal kernel smoothing function, h is the data points sampling bandwidth, n is the total number of data points with x_i representing each data point, and x is the sampling position. The probability density of these values (average von Mises stress or coordination number) is determined and plotted against the deposition rate. Further, the comparison of the mesoscopic characteristics of small-sized powders (D_{m} = 50 µm) and large-sized powders (D_{m} = 100 µm) is presented here. The colour intensity shows the probability density values, which means the higher the intensity, the higher the density of the values.

3.1.2 Stress distribution of the powder particles in the pile

For mean particle size of 50 µm, average von Mises stresses are less at lower surface energy (γ = 0.25 mJ/m^2), leading to higher deposition rates. These stresses and deposition rates of the three models are similar, as indicated by the blue circle in Fig. 9a. With increasing the surface energy (γ), cohesive forces among the powder particles increase, leading to lower deposition rates and higher stresses. This can be observed for cohesive powders (γ = 2.5 mJ/m^2), as depicted by the blue to red circles in Fig. 9b. As mentioned in Sect. 2, the DMT model predicts higher cohesive forces than the JKR model, stresses in the pile obtained from DMT are higher than the JKR (red and green circle in Fig. 9b, respectively). For mean particle size of 100 µm, at lower surface energy, stress (σ_{v}) is lower, similar to 50 µm; however, the deposition is higher due to large size and lower cohesive forces (compare Fig. 9a, c). Additionally, for large-sized powders (D_{m} = 100 µm), the variation of the stresses with deposition rates at higher surface energy is not observed (within the range of values considered), as shown in Fig. 9d.

3.1.3 Coordination number distribution of the powder particles

The coordination number of the powder particles provides insights into the flowability and spreadability of the powders. At lower surface energy (γ = 0.25 mJ/m^2), powder with a mean size of 50 µm, the average coordination number, and deposition rates of all the three models are similar, as shown in Fig. 10a. With an increase in the surface energy, the coordination number and deposition rate decreases for the small-sized powders, as shown in Fig. 10b. Figure 10c depicts the coordination number for large-sized (D_{m} = 100 µm) and small-sized (D_{m} = 50 µm) particles at low surface energy. At low surface energy, with a decrease in the particle size, the coordination number increases. With an increase in the surface energy, the coordination number is unaltered for large particles (within the range of values considered). In contrast, with an increase in the surface energy, the coordination number decreases for the small-sized powders (see Fig. 10d). In summary, with the decrease in particle sizes, the coordination number increases initially. Further decrease in the mean particle size, coordination number decreases as the cohesive forces lead to agglomerations or cluster formation in the pile, as reported by He et al. [36].

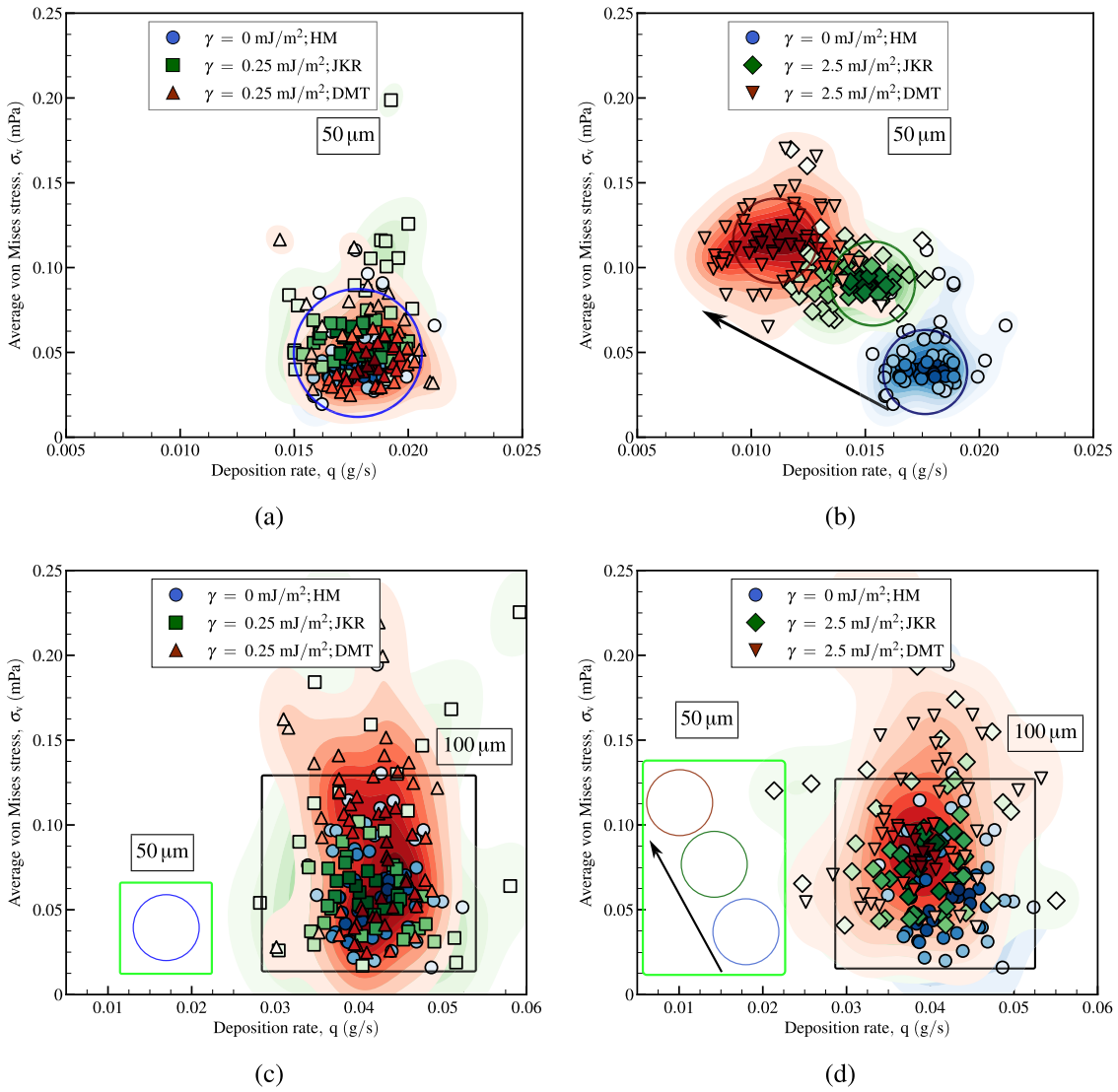

Fig. 9 Stress distribution (σ_v) with deposition rate (q) for different models and surface energies (γ). For mean particle size of 50 μm **a** low surface energy (γ = 0.25 mJ/m^2) **b** high surface energy (γ = 2.5 mJ/m^2). Comparison between mean particle size of 50 μm and 100 μm **c** low surface energy (γ = 0.25 mJ/m^2) and **d** high surface energy (γ = 2.5 mJ/m^2). For ease of comparison, the stresses of D_m = 50 μm are represented with the similar coloured circles in the green box in **c** and **d**

3.2 Effect of the standard deviation of the powder sizes on the bed quality

In PBFAM, powders may exhibit varying particle size distributions. These distributions are categorized as well graded and poorly graded. Well-graded powders refer to those with a wide range of particle sizes, with particles of different sizes. On the other hand, poorly graded powders are closer to being mono-sized, meaning particles have a uniform size distribution. In this section, the effect of standard deviation (S_D) of the powder sizes on the powder bed quality is analysed. The mean size of the powder is chosen to be 50 μm, and different standard deviations like 1, 3, and 5 are used for the simulations, as shown in Fig. 11a. The particle size distribution with a standard deviation of 1 are poorly graded, whereas PSD with a standard deviation of 5 is a relatively well-graded system. Similar to Sect. 3.1, several simulations are carried out with varying surface energies (γ) of the particles and with the HM, JKR, and DMT contact models.

3.2.1 Average packing fraction and homogeneity of the powder layer

The variation of the packing fraction of the spread layer with respect to γ is shown in Fig. 11b. As mentioned in Sect. 3.1.1, the packing fraction of the spread powder layer

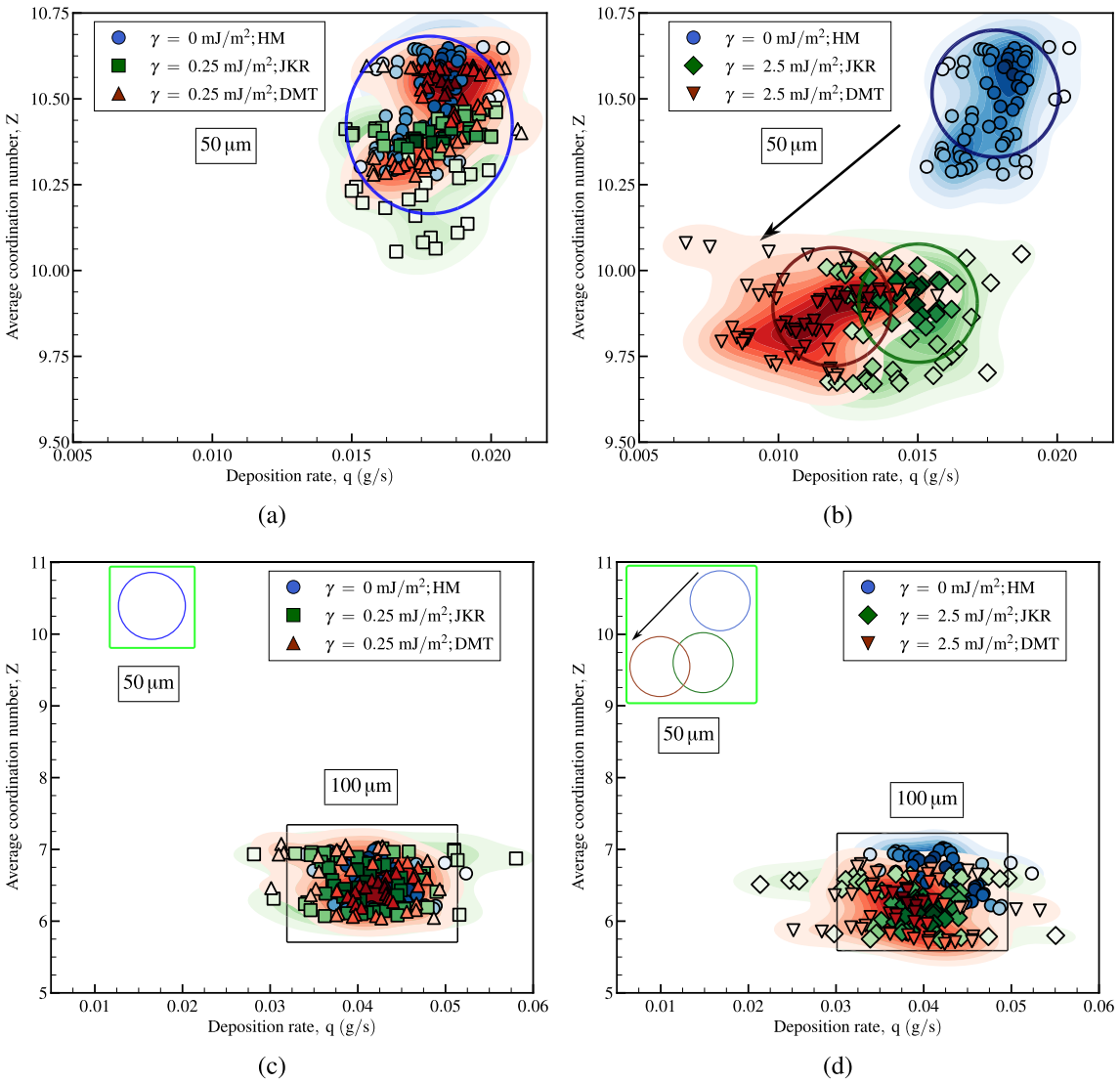

Fig. 10 Coordination number (Z) distribution with deposition rate (q) for different models and surface energies (γ). For mean particle size of 50 μm **a** low surface energy (γ = 0.25 mJ/m^2) **b** high surface energy (γ = 2.5 mJ/m^2). Comparison between mean particle size of 50 μm and 100 μm **c** low surface energy (γ = 0.25 mJ/m^2) and **d** high surface energy (γ = 2.5 mJ/m^2). For ease of comparison, the coordination number distribution of D_m = 50 μm is represented with the similar coloured circles in the green box in **c** and **d**

is independent of the surface energy for the HM model (solid lines in Fig. 11b). As the S_D increases, particle size difference increases so that the small particles occupy the voids, thereby increasing the packing fraction of the bed. It is well known that as standard deviation increases, the packing fraction of the system increases (polydispersity in [57]). As mentioned in Sect. 3.1.1, for JKR and DMT models, the packing fraction of the bed decreases with increasing γ (dashed lines for JKR and dashed dot with marker lines for DMT in Fig. 11b). As the S_D increases, resulting in an increased number of smaller particles. Consequently, these smaller particles increase cohesive forces in the system. The cohesive forces reduce the flowability and spreadability of the powder, and thereby, the packing fraction of the powder layer decreases with increasing S_D, as shown in Fig. 11b. As the DMT model detects higher cohesive forces than the JKR model, as described in Sect. 2, the packing fraction obtained by the DMT model is lower than the JKR model.

3.2.2 Stress and coordination number distribution of the powder particles in the pile

With the decrease in the standard deviation of the powder sizes, the powder behaves less cohesive. As a result, powders have higher deposition and lower stress. For powders with S_D = 1, at lower surface energy, the deposition rate and

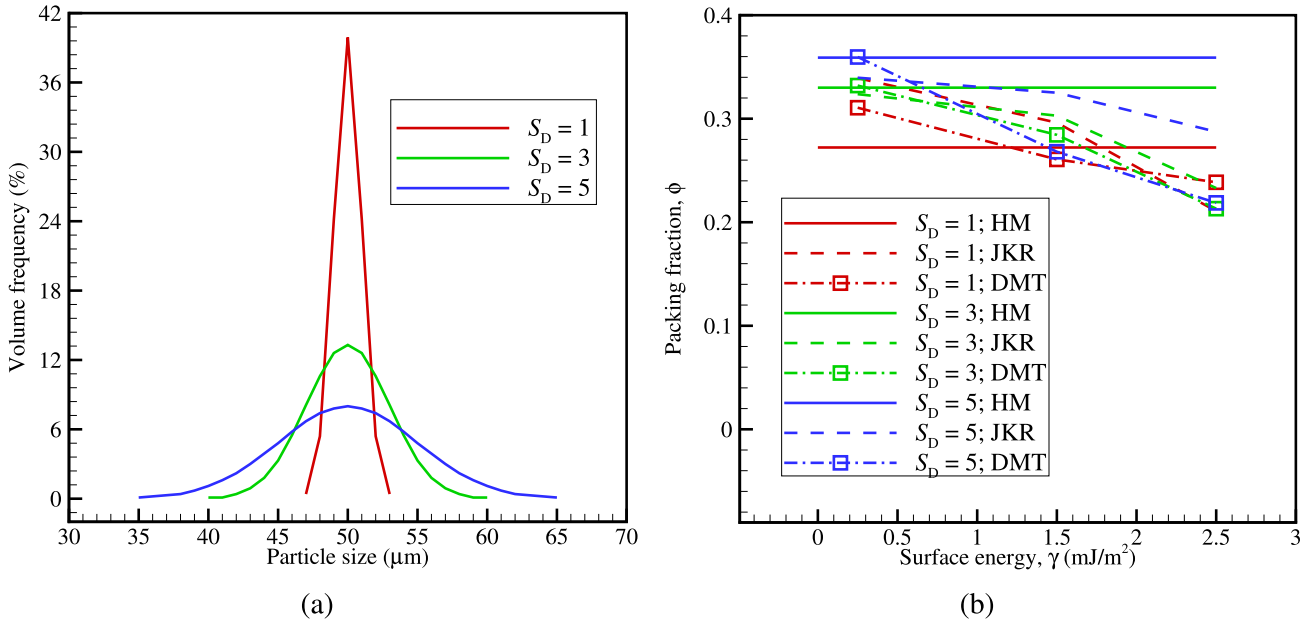

Fig. 11 **a** Particle size distribution for different standard deviations (S_D), and **b** packing fraction (ϕ) variation as a function of the surface energy (γ)

average von Mises stresses of the cohesion models (JKR and DMT) are similar to the HM. With the increase in the surface energy, cohesive forces increase, leading to lower deposition and higher average von Mises stresses as shown in Fig. 12a. However, the increase in the stresses and decrease in deposition for powders with $S_D = 1$ are lower than $S_D = 5$, as shown in Fig. 12b. With the increase in the surface energy, a decrease in the average coordination number is also observed for powders with $S_D = 1$, as shown in Fig. 12c. This characteristic is similar to the powders with $S_D = 5$ (see Fig. 10b). However, coordination number distribution is too scattered for powders with $S_D = 1$, and this implies low cohesivity of the powders. As the S_D increases, small-sized particles increase relatively. Thereby, the coordination number increases for powders with higher S_D, as shown in Fig. 12d.

3.3 Suitability of the contact model based on the Tabor parameter

In this section, the suitability of Tabor's parameter range as a guideline for the selection of a specific cohesion model (JKR or DMT) for powder spreading simulations is investigated. Several simulations are carried out to study the combined effect of the elastic modulus and the surface energy, as shown in Table 3. The range of Young's modulus and surface energy considered in this study is based on values extracted from relevant literature, as presented in Table 1. Figures 13a, b depict the variation of the packing fraction of the spread layer with $\log(\lambda_T)$ for JKR and DMT models, respectively. It can be observed that with an increase in the $\log(\lambda_T)$, the packing fraction decreases in both models as the particles become softer and more cohesive. The difference between the packing fraction obtained from the models is calculated using the root mean square deviation (RMSD), as given in Eq. (3.4).

$$\text{RMSD} = \sqrt{\frac{\sum_{i=1}^{n} \left(\frac{\phi_{\text{i,JKR}} - \phi_{\text{i,DMT}}}{\phi_{\text{i,DMT}}} \right)^2}{n}} \tag{3.4}$$

where $\phi_{\text{i,JKR}}$, and $\phi_{\text{i,DMT}}$ are the packing fraction of the spread layer obtained using JKR and DMT models, respectively, and n is the number of realisations. The structure of the powder layer is generally evaluated by metrics such as packing fraction, coordination number and particle clustering [36]. The present study uses the packing fraction to assess the layer structure. Figure 13c depicts a variation of RMSD as a function of the packing fraction of the spread layer. As mentioned in Sect. 2.2, the JKR model is valid for $\log(\lambda_T) > 0.5$, and the DMT model is more appropriate for $\log(\lambda_T) < -1$. However, the RMSD variation of the packing fraction gives a different perspective. The RMSD between the models is very close to zero for $\log(\lambda_T) < -1$, and deviation increases with an increase in $\log(\lambda_T)$, as shown in Fig. 13c. Both the models depict similar layer structures for lower values of λ_T and different structures with an increase in λ_T. At lower values of λ_T, both the JKR and DMT models yield similar packing fractions because the interaction between particles is less influenced by the cohesion. In this range, the forces predicted by both the models are nearly equivalent, making either model suitable for simulations in low λ_T ranges. How-

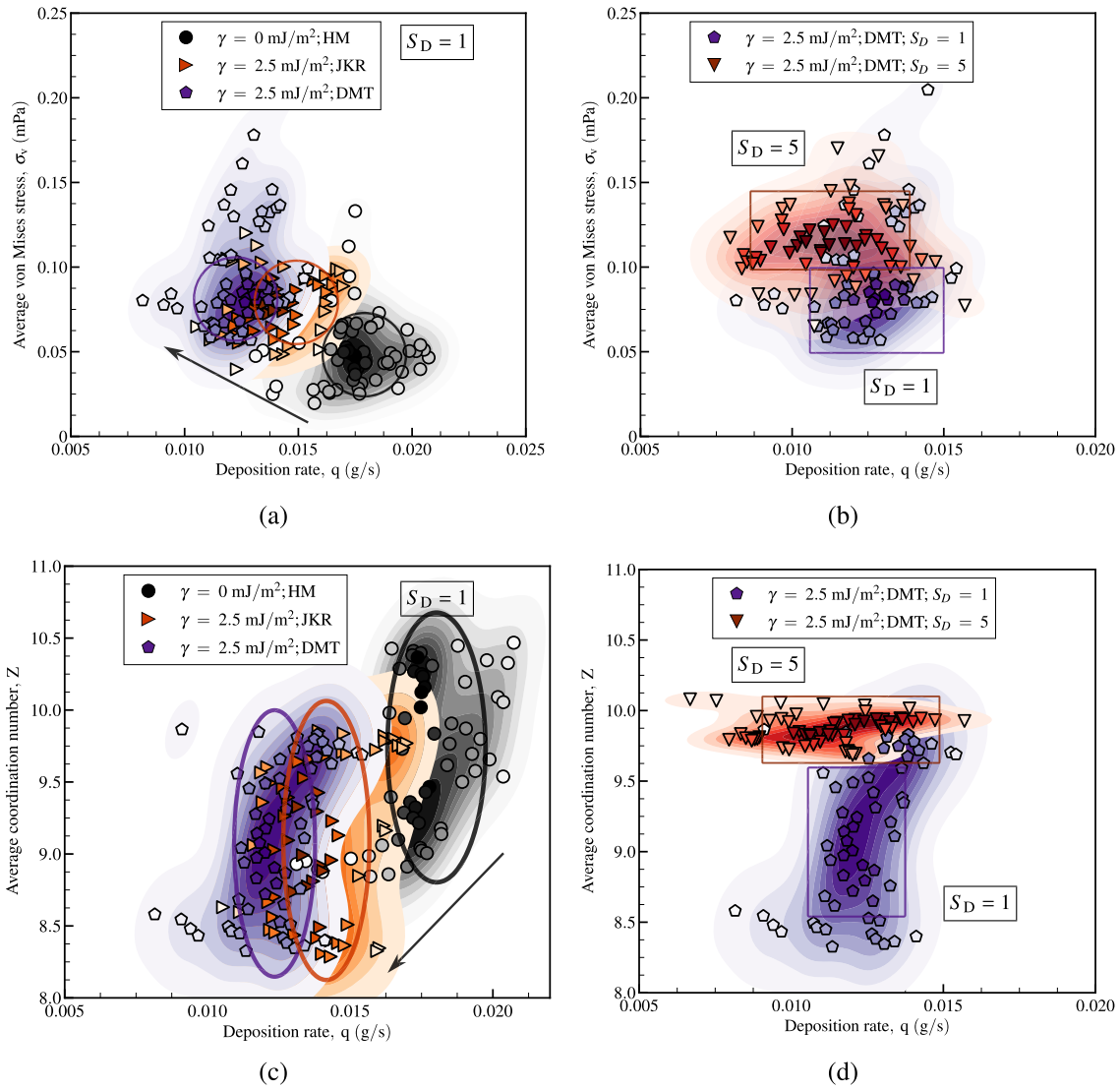

Fig. 12 Average von Mises stress (σ_v) distribution with respect to deposition rate (q) for different models and surface energies **a** with a standard deviation of 1 **b** comparison between $S_D = 1$ and $S_D = 5$. Coordination number (Z) distribution with respect to deposition rate (q) for different models and surface energies **c** with a standard deviation of 1 **d** comparison between $S_D = 1$ and $S_D = 5$

ever, at higher λ_T values, particles become relatively softer (see Young's modulus values in Table 3) and are highly influenced by cohesive forces, causing the contact forces between the two models to diverge and resulting in different layer structures. This analysis is consistent with recent findings by Greenwood [58], where the author highlighted that the DMT model focused primarily on calculating the pull-off force during cohesion, but it did not provide a comprehensive description of contact mechanics like the JKR model. Further, Greenwood [58] also identified errors in the thermodynamic formulation of the DMT model and argued that Hertzian geometry does not occur as assumed in the DMT theory. Therefore, the JKR model is more suitable and can be applied across the entire range of the Tabor parameter.

4 Conclusions

In this work, DEM simulations were carried out to analyse powder spreading dynamics with a focus on additive manufacturing, considering the HM, JKR, and DMT contact models. The results demonstrate that both the mean and standard deviation of the powder sizes significantly influence the powder layer quality. A decrease in the mean size or increase in the standard deviation of the powder sizes reduces their spreadability, resulting in a lower packing fraction that is accurately captured by both the JKR and DMT models. Additionally, the Hertz–Mindlin (HM) contact model was found to be inadequate for simulating powders with mean sizes smaller than 100 μm, as it does not capture the cohe-

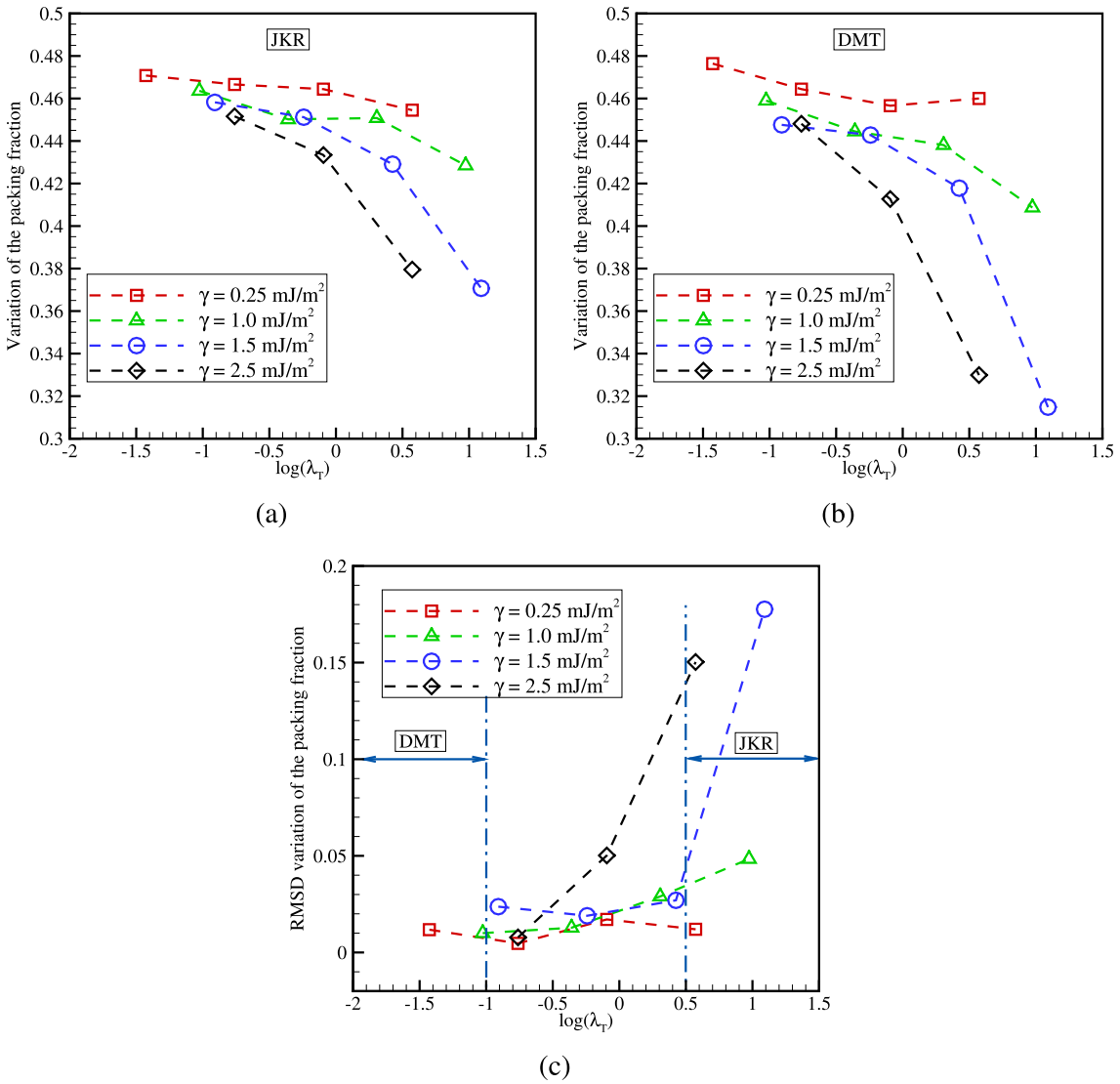

Fig. 13 Variation of packing fraction vs $\log(\lambda_T)$ for **a** JKR and **b** DMT models **c** RMSD of the packing fraction for both models

Table 3 List of cases for parametric analysis of surface energy and Young's modulus for powders with $D_m = 50\,\mu m$

Surface energy (γ, mJ/m^2)	Young's modulus (E, GPa)	Tabor's parameter (λ_T)	$\log(\lambda_T)$
0.25	210	0.037	−1.40
1.0	210	0.0942	−1.046
1.5	210	0.12	−0.92
2.5	210	0.17	−0.77
0.25	21	0.17	−0.77
1.5	21	0.57	−0.244
2.5	21	0.8	−0.092
0.25	2.1	0.8	−0.09
1.5	2.1	2.66	0.43
2.5	2.1	3.74	0.573
0.25	0.21	3.74	0.573
1.5	0.21	12.3	1.09

sive behaviour of these fine powders. This insight suggests that cohesive contact models, JKR and DMT, are essential for accurately predicting powder layer behaviour.

The deposition mechanism is characterised by average von Mises stress (σ_v) and coordination number (Z). With an increase in surface energy, the spreadability of the powder reduces, resulting in a lower deposition rate. Additionally, the average von Mises stress within the powder pile increases, while the coordination number decreases with the increase in surface energy. This trend is observed only for powders with mean sizes smaller than 100 μm, due to the influence of cohesive forces.

The suitability of Tabor's parameter range as a criterion for the selection of an appropriate cohesion model is investigated. For the lower Tabor's parameter, both the JKR and DMT models predict similar powder layer structure. However, for the higher values of Tabor's parameter, the contact forces for the JKR and DMT models diverge and generate different structures. Hence, either the JKR or DMT model can be used in the lower range of the Tabor parameter ($\lambda_T < 0.1$), and for powders with material properties exhibiting higher Tabor parameter ($\lambda_T > 3$, relatively low elastic modulus, large size, or high surface energy), only the JKR model is appropriate. Using the DMT model for materials with a higher Tabor parameter can lead to an overestimation of cohesive forces, resulting in inaccurate predictions of powder behaviour. Through this study, we emphasize that the JKR model can be applied across the entire range of the Tabor parameter, consistent with the fundamental insights of Greenwood [58].

The detailed investigation of the two cohesion contact models demonstrates that the JKR model can be effectively applied to a wide variety of powder types, provided the material properties are appropriately defined for each case. The versatility of this contact model makes it suitable for simulating various powder behaviours across different industries, including additive manufacturing, pharmaceuticals, and ceramics.

Supplementary Information The online version contains supplementary material available at https://doi.org/10.1007/s40571-024-00894-w.

Acknowledgements The authors thankfully acknowledge the generous research funding and simulation resources provided by Altair India Private Limited. The authors also acknowledge the generous financial support from IIT Madras under the Institutes of Eminence (IoE) scheme funded by the Ministry of Education, Government of India.

Data Availability Data will be made available on reasonable request.

Declarations

Conflict of interest The authors declare that they have no conflict of interest.

References

1. DebRoy T, Wei H, Zuback J, Mukherjee T, Elmer J, Milewski J, Beese AM, Wilson-Heid A, De A, Zhang W (2018) Additive manufacturing of metallic components–process, structure and properties. Prog Mater Sci 92:112–224
2. Karunakaran K, Bernard A, Suryakumar S, Dembinski L, Taillandier G (2012) Rapid manufacturing of metallic objects. Rapid Prototyp J
3. Huang R, Riddle M, Graziano D, Warren J, Das S, Nimbalkar S, Cresko J, Masanet E (2016) Energy and emissions saving potential of additive manufacturing: the case of lightweight aircraft components. J Clean Prod 135:1559–1570
4. Fateri M, Kaouk A, Cowley A, Siarov S, Palou MV, González FG, Marchant R, Cristoforetti S, Sperl M (2018) Feasibility study on additive manufacturing of recyclable objects for space applications. Addit Manuf 24:400–404
5. Murr L (2020) Metallurgy principles applied to powder bed fusion 3D printing/additive manufacturing of personalized and optimized metal and alloy biomedical implants: an overview. J Market Res 9:1087–1103
6. Parteli EJ, Pöschel T (2016) Particle-based simulation of powder application in additive manufacturing. Powder Technol 288:96–102
7. Averardi A, Cola C, Zeltmann SE, Gupta N (2020) Effect of particle size distribution on the packing of powder beds: a critical discussion relevant to additive manufacturing. Mater Today Commun 24:100964
8. Steen W, Dowden J, Davis M, Kapadia P (1988) A point and line source model of laser keyhole welding. J Phys D Appl Phys 21:1255
9. Yuan P, Gu D (2015) Molten pool behaviour and its physical mechanism during selective laser melting of TiC/AlSi10Mg nanocomposites: simulation and experiments. J Phys D Appl Phys 48:035303
10. Körner C, Attar E, Heinl P (2011) Mesoscopic simulation of selective beam melting processes. J Mater Process Technol 211:978–987
11. Lee Y, Zhang W (2016) Modeling of heat transfer, fluid flow and solidification microstructure of nickel-base superalloy fabricated by laser powder bed fusion. Addit Manuf 12:178–188
12. Escano LI, Parab ND, Xiong L, Guo Q, Zhao C, Fezzaa K, Everhart W, Sun T, Chen L (2018) Revealing particle-scale powder spreading dynamics in powder-bed-based additive manufacturing process by high-speed X-ray imaging. Sci Rep 8:1–11
13. Parteli EJ, Schmidt J, Blümel C, Wirth K-E, Peukert W, Pöschel T (2014) Attractive particle interaction forces and packing density of fine glass powders. Sci Rep 4:6227
14. Xiang Z, Yin M, Deng Z, Mei X, Yin G (2016) Simulation of forming process of powder bed for additive manufacturing. J Manuf Sci Eng 138:081002
15. Chen H, Wei Q, Zhang Y, Chen F, Shi Y, Yan W (2019) Powder-spreading mechanisms in powder-bed-based additive manufacturing: experiments and computational modeling. Acta Mater 179:158–171
16. Nan W, Ghadiri M (2019) Numerical simulation of powder flow during spreading in additive manufacturing. Powder Technol 342:801–807
17. Yim S, Bian H, Aoyagi K, Yamanaka K, Chiba A (2022) Spreading behavior of Ti48Al2Cr2Nb powders in powder bed fusion additive manufacturing process: experimental and discrete element method study. Addit Manuf 49:102489
18. Wu S, Lei Z, Jiang M, Liang J, Li B, Chen Y (2022) Experimental investigation and discrete element modeling for particle-scale powder spreading dynamics in powder-bed-fusion-based additive manufacturing. Powder Technol 403:117390

19. Yao D, An X, Fu H, Zhang H, Yang X, Zou Q, Dong K (2021) Dynamic investigation on the powder spreading during selective laser melting additive manufacturing. Addit Manuf 37:101707
20. Shaheen MY, Thornton AR, Luding S, Weinhart T (2021) The influence of material and process parameters on powder spreading in additive manufacturing. Powder Technol 383:564–583
21. Xu R, Nan W (2023) Analysis of the metrics and mechanism of powder spreadability in powder-based additive manufacturing. Addit Manuf 71:103596
22. Marchais K, Girardot J, Metton C, Iordanoff I (2021) A 3D DEM simulation to study the influence of material and process parameters on spreading of metallic powder in additive manufacturing. Comput Part Mech 8:943–953
23. Cundall PA, Strack OD (1979) A discrete numerical model for granular assemblies. Geotechnique 29:47–65
24. O'Sullivan C (2011) Particulate discrete element modelling: a geomechanics perspective. CRC Press, Cambridge
25. Antonyuk S (2019) Particles in contact: micro mechanics, micro process dynamics and particle collective. Springer, Berlin
26. Ji S, Liu L (2020) Computational granular mechanics and its engineering applications. Springer, Berlin
27. Thornton C (2015) Granular dynamics, contact mechanics and particle system simulations, vol 24. Springer, Berlin
28. Wang L, Li E, Shen H, Zou R, Yu A, Zhou Z (2020) Adhesion effects on spreading of metal powders in selective laser melting. Powder Technol 363:602–610
29. Haeri S, Wang Y, Ghita O, Sun J (2017) Discrete element simulation and experimental study of powder spreading process in additive manufacturing. Powder Technol 306:45–54
30. Han Q, Gu H, Setchi R (2019) Discrete element simulation of powder layer thickness in laser additive manufacturing. Powder Technol 352:91–102
31. Chen H, Wei Q, Wen S, Li Z, Shi Y (2017) Flow behavior of powder particles in layering process of selective laser melting: numerical modeling and experimental verification based on discrete element method. Int J Mach Tools Manuf 123:146–159
32. Nan W, Pasha M, Bonakdar T, Lopez A, Zafar U, Nadimi S, Ghadiri M (2018) Jamming during particle spreading in additive manufacturing. Powder Technol 338:253–262
33. Wu Q, Qiao C, Wang J, Yao D, Wu Y, Fan W, Li M, An X (2022) Adaptability investigations on bottom modified blade in powder spreading process of additive manufacturing. Addit Manuf 49:102477
34. Meier C, Weissbach R, Weinberg J, Wall WA, Hart AJ (2019) Modeling and characterization of cohesion in fine metal powders with a focus on additive manufacturing process simulations. Powder Technol 343:855–866
35. Yuksel A, Cullinan M (2016) Modeling of nanoparticle agglomeration and powder bed formation in microscale selective laser sintering systems. Addit Manuf 12:204–215
36. He Y, Hassanpour A, Bayly AE (2020) Linking particle properties to layer characteristics: discrete element modelling of cohesive fine powder spreading in additive manufacturing. Addit Manuf 36:101685
37. Gao X, Zhang L, Zhang Z (2024) Compatibility of tool geometry and process parameters in powder bed fusion. Comput Part Mech 1–16
38. Chen J, Krengel D, Nishiura D, Furuichi M, Matuttis H-G (2023) A force-displacement relation based on the JKR theory for DEM simulations of adhesive particles. Powder Technol 427:118742
39. Ye Y, Zeng Y, Sun H, Chen X, Cheng S, Ma W (2021) An experimental and theoretical study of the cyclic contact behaviour for rock sphere. Powder Technol 385:375–385
40. Korayem M, Taheri M (2014) Modeling of various contact theories for the manipulation of different biological micro/nanoparticles based on AFM. J Nanopart Res 16:1–18
41. Korayem M, Khaksar H (2020) A survey on dynamic modeling of manipulation of nanoparticles based on atomic force microscope and investigation of involved factors. J Nanopart Res 22:27
42. Behjani MA, Rahmanian N, Hassanpour A et al (2017) An investigation on process of seeded granulation in a continuous drum granulator using DEM. Adv Powder Technol 28:2456–2464
43. Pizette P, Martin CL, Delette G, Sans F, Geneves T (2013) Green strength of binder-free ceramics. J Eur Ceram Soc 33:975–984
44. Behjani MA, Motlagh YG, Bayly AE, Hassanpour A (2020) Assessment of blending performance of pharmaceutical powder mixtures in a continuous mixer using discrete element method (DEM). Powder Technol 366:73–81
45. Hertz H (1881) The contact of elastic solids. Journal für die reine und angewandte Mathematik 92:156–171
46. Mindlin R (1949) Elastic spheres in contact under varying oblique forces. J Appl Mech 16:327–330
47. Johnson KL, Kendall K, Roberts A (1971) Surface energy and the contact of elastic solids. Proc R Soc Lond A Math Phys Sci 324:301–313
48. Hamaker HC (1937) The London-van der Waals attraction between spherical particles. Physica 4:1058–1072
49. Derjaguin BV, Muller VM, Toporov YP (1975) Effect of contact deformations on the adhesion of particles. J Colloid Interface Sci 53:314–326
50. Hærvig J, Kleinhans U, Wieland C, Spliethoff H, Jensen AL, Sørensen K, Condra TJ (2017) On the adhesive JKR contact and rolling models for reduced particle stiffness discrete element simulations. Powder Technol 319:472–482
51. Tabor D (1977) Surface forces and surface interactions. J Colloid Interface Sci 58:2–13
52. Greenwood J (1997) Adhesion of elastic spheres. Proc R Soc Lond Ser A Math Phys Eng Sci 453:1277–1297
53. Maugis D (1992) Adhesion of spheres: the JKR-DMT transition using a Dugdale model. J Colloid Interface Sci 150:243–269
54. Xu D, Liechti KM, Ravi-Chandar K (2007) On the modified tabor parameter for the JKR–DMT transition in the presence of a liquid meniscus. J Colloid Interface Sci 315:772–785
55. Altair EDEM, 2022. https://help.altair.com/EDEM/Introducing_EDEM.htm
56. Nan W, Gu Y (2022) Experimental investigation on the spreadability of cohesive and frictional powder. Adv Powder Technol 33:103466
57. Jaggannagari SR, Desu RK, Reimann J, Gan Y, Moscardini M, Annabattula RK (2021) DEM simulations of vibrated sphere packings in slender prismatic containers. Powder Technol 393:31–59
58. Greenwood J (2022) Derjaguin and the DMT theory: a farewell to DMT? Tribol Lett 70:61

Publisher's Note Springer Nature remains neutral with regard to jurisdictional claims in published maps and institutional affiliations.

Springer Nature or its licensor (e.g. a society or other partner) holds exclusive rights to this article under a publishing agreement with the author(s) or other rightsholder(s); author self-archiving of the accepted manuscript version of this article is solely governed by the terms of such publishing agreement and applicable law.